

Group theoretical and *ab-initio* description of color center candidates in fluorographene

M. S. Tacca^{1,*} and M. B. Plenio^{1,†}

¹*Institut für Theoretische Physik and IQST, Albert-Einstein-Allee 11, Universität Ulm, D-89081 Ulm, Germany.*

(Dated: July 12, 2023)

We present a group theoretical and *ab-initio* analysis of lattice point defects in fluorographene, with a focus on neutral and negative V_{CF} vacancies. By using a combination of density functional theory calculations and group theory analysis, we investigate the many-body configurations of the defects and calculate the vertical absorption and zero-phonon line energies of the excited states and their dependence with strain. The description of the defects is extended by computing their formation energy, as well as further relevant parameters as the Jahn-Teller energy for neutral V_{CF} and the zero field splitting for negative V_{CF} vacancies. Based on our results, we discuss possible quantum applications of these color centers when coupled to mechanical oscillation modes of the hosting two-dimensional material. The symmetry and active orbitals of the defects exhibit a parallelism with those of the extensively studied NV centers in diamond. In this context, the studied defects emerge as interesting candidates for the development of two-dimensional quantum devices based on fluorographene.

I. INTRODUCTION

Point defects are of increasing interest in the fields of quantum information and sensing due to their potential applications, among which are the promising NV center technologies [1–3]. By coupling the localized states introduced by color centers with mechanical oscillation modes, hybrid quantum devices with long-range interactions mediated by phonons can be fabricated through appropriate design [4–8]. The introduction of color centers in two-dimensional (2D) materials is particularly promising for the continuously accelerated development of quantum technologies.

Two-dimensional resonators can be mechanically coupled with cavities through opto-thermal, electromagnetic, or further interactions [9–11]. The dynamics of 2D membranes and other micro- and nano-devices have been widely studied for their potential applications in quantum and mass sensors, quantum simulators, and nanophotonics [10, 12–14]. Because color centers in 2D structures lie naturally on the surface of the material, high sensitivity to the environment is expected [15]. Various materials, including graphene [16–19], MoS_2 [20, 21], hexagonal boron nitride (h-BN) [22, 23] and others [10, 24, 25] have been studied as candidates for 2D systems. In particular, h-BN, a wide-band insulator that can host color centers [26, 27], has been proposed as a platform for quantum simulation and ultra-sensitive force detection [22, 23, 28, 29].

In this work, we explore the potential of defect-bearing fluorographene [30, 31] as a platform for the realization of hybrid quantum devices. Fluorographene (FG) is a stoichiometric 2D derivative of graphene, in which one fluorine atom is bonded to each carbon atom. This material has been used for a variety of applications, including electrochemical sensors, batteries, and electrocatalysis, as well as electronic applications such as transistors and solar cells [32]. A key characteristic of FG is that the carbon atoms exhibit sp_3 hybridization instead of the sp_2 one found in graphene. As a result, the electronic properties of FG are closer to those of diamond than to those of

graphite. In fact, the structure of FG is similar to the fluorine-terminated (111) diamond surface, which has been proposed as a suitable candidate for the implementation of a quantum simulator at room temperature [33]. The application of polarized nuclear spins in quantum simulators is an active research field, in particular for the previously mentioned h-BN based systems [34, 35].

Although it has been well established that FG presents a large band gap, its precise value has been a longstanding issue that appears to have been clarified only recently [36]. Initial measurements suggested a band gap larger than 3 eV [31], and latter measurements yielded a value of 3.8 eV, consistent with the first results [37]. Additional photoluminescence emission peaks have been observed at 3.56 [38] and 3.65 eV [37, 38], with the latter being attributed to phonon-assisted radiative recombination. On the theoretical field, the initial density functional theory (DFT) [39] calculations at the local density approximation (LDA) and generalized gradient approximation (GGA) theory levels resulted in predicted band gap values close to 3 eV [40–44], in excellent agreement with the experimental measurements. However, more refined calculations including the exact exchange interaction through the hybrid screened functional (HSE) predicted a larger band gap of ≈ 5 eV [43, 45].

Additional calculations incorporating electron-electron interactions via Green’s function methods (GW) on top of either LDA or GGA to further improve the description of the electronic structure, led to a predicted band gap of about 7.5 eV [41, 42, 44, 45]. The inclusion of electron–hole interactions through the Bethe–Salpeter equation (BSE–GW), one of the most advanced methods beyond DFT, partially cancels the electron–electron interactions and results in predicted band gap values between 5.4 [44] and 5.65 eV [36]. It is worth noting that the latter values are in agreement with the results obtained via the HSE method, which is computationally less demanding.

The discrepancies between the measured and calculated values of the band gap have been tentatively linked to midgap states resulting from defects in the material [42, 44]. A combined experimental and theoretical study has confirmed this hypothesis, showing that the band gap value is in agreement with previously reported BSE–GW results [36]. The long-

* marcos.tacca@uni-ulm.de

† martin.plenio@uni-ulm.de

standing FG bandgap conundrum highlights the importance of characterizing defects in materials. However, most theoretical works on FG have primarily focused on improving the accuracy of band gap predictions for the pristine material. Thus, the calculation of defects is often relegated to a secondary place [44–46], or analyzed at the GGA level of the theory, which strongly underestimates the band gap [47].

In this work, we investigate the electronic structure of two types of defects in FG: a F vacancy (V_F) and a double F and C vacancy (V_{CF}), for which different charge states were considered. The paper is structured as follows. We present the description of the theoretical method in Section II. Our approach involves using DFT to obtain the single-particle localized states and group theory to construct the many-body configurations. In Section III we discuss our results. We start with a description of pristine fluorographene and the V_F defect in Section III A. Neutral and negative V_{CF} vacancies are presented in Sections III B and III C. We examine the transitions between ground and excited states introduced by the defects and analyze their dependence on strain. In addition, we compute the Jahn-Teller energy for the neutral defect and the zero field splitting for the negatively charged one. Given that the symmetry of the V_{CF} defect is equivalent to that of a NV center, a parallelism can be established between both systems. Based on previous NV studies, in Section III D we discuss possible applications of defective FG sheets as quantum hybrid resonators. Our calculations of the formation energy of the defects are presented in Section III E. The conclusions are presented in Section IV.

II. METHODS

The computational details of our work, based on previous studies of related 2D systems [15, 48, 49], are as follows. We employed the DFT code Quantum Espresso [50] and used a supercell approach to study defects in FG. We used the HSE method with PBE functional [51, 52], adjusting the parameter $\alpha = 0.35$ to match the band gap of fluorographene obtained with the latest calculations and experimental data [36]. In order to perform geometrical relaxations including HSE, we used norm conserving pseudopotentials. We used an energy cutoff of 100 Ry and, unless otherwise stated, we used a value of 0.01 eV/Å as criterion for the convergence of the atomic forces. We considered a 15 Å vacuum spacing between fluorographene sheets.

For our calculations we considered 7×7 hexagonal supercells to avoid interaction between defects. For the calculations involving strain in x and y directions we used 7×8 orthogonal supercells. In both cases we considered only the Γ point in the reciprocal space and therefore a single q point in the Hartree-Fock calculation for the HSE method.

In our study, we employed the Δ SCF method [53, 54] to calculate relevant transition energies, which involves computing the energy difference between the ground state and excited states with different electronic occupations. We determined the vertical absorption energy (VAE) by keeping the ground state geometry fixed and imposing an excited electronic oc-

cupation for the calculation of the excited states. The zero-phonon line (ZPL) was obtained after performing a geometrical relaxation of the excited electronic configuration. It should be noted that the Δ SCF method is applicable only to configurations corresponding to a single Slater determinant. To estimate the energy of multi-determinantal configurations, we used auxiliary single-determinant states [55, 56]. It is worth stressing that this method provides only an estimation of the transition energies for such configurations [57, 58].

III. RESULTS

A. Pristine fluorographene and V_F

We obtained a lattice parameter of 2.58 Å for pristine fluorographene, in good agreement with available theoretical [42, 59, 60] and experimental [31, 61] data, and a band-gap of 5.65 eV.

We start our analysis of defects with the simple fluorine vacancy, V_F , which lowers the C_{6v} symmetry of pristine fluorographene to C_{3v} . The V_F vacancy leaves a C atom with a dangling sp^3 bond, which corresponds directly to a molecular orbital (MO) with spatial symmetry A_1 . We denoted this single-electron orbital a_1 . The geometry of the system and the a_1 orbital are illustrated in Fig. 1(a).

According to our spin-polarized DFT calculation, the a_1 orbital is half occupied in the ground state (GS), resulting in a magnetic moment of the defect of 1 and a 2A_1 many-body configuration. The molecular orbitals of the majority (up) and minority (down) spins are well localized, with the up state located within the valence band and the down state inside the band gap (see Fig. 1(b)). The first excited state (ES) can be constructed by promoting an electron from the highest occupied valence bands, which have E symmetry, to the unoccupied a_1 state. In this case, the well-localized a_1 orbital is doubly occupied, and there is a single hole in the E bands.

We calculated the VAE and ZPL following the methodology described in Section II, and obtained values of 3.44 eV and 3.00 eV, respectively. The ZPL value is consistent with absorption bands observed in less fluorinated fluorographene samples [36]. As suggested in Ref. [36], it is likely that the optical transitions introduced by this midgap state were initially attributed to a much lower band-gap of fluorographene.

B. V_{CF}

A V_{CF} defect in fluorographene also lowers the symmetry of the system to C_{3v} . In this case, there are three sp^3 dangling bonds of the C atoms around the defect, and an in-depth group-theory analysis becomes relevant. Using the projection operator method [62] we determined that the three localized orbitals that can be formed have symmetries A_1 and E . The

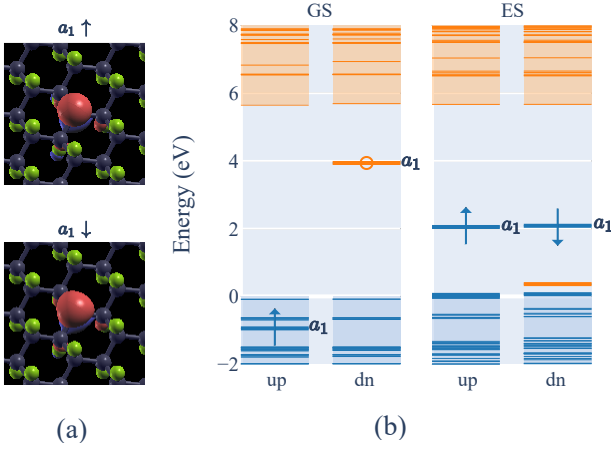


FIG. 1. (a) Geometry of fluorographene with a V_F vacancy and the localized a_1 orbital. (b) Single-particle levels for the ground state (GS) and excited state (ES) of the V_F vacancy. The occupied (empty) single-electron states are indicated in blue (orange), and the conduction (valence) bands are shown as areas shaded with the same colors. The localized orbitals are labeled, and their occupancy is indicated with symbols: empty (circle) or occupied (up or down arrows).

single-particle orbitals a_1 , e_x and e_y are given by

$$a_1 = \frac{1}{\sqrt{3}}(\sigma_1 + \sigma_2 + \sigma_3) \quad (1)$$

$$e_x = \frac{1}{\sqrt{6}}(2\sigma_1 - \sigma_2 - \sigma_3) \quad (2)$$

$$e_y = \frac{1}{\sqrt{2}}(\sigma_2 - \sigma_3), \quad (3)$$

where σ_i corresponds to the dangling orbital of each C atom. The geometry of the system and the orbitals is presented in Fig. 2(a).

The most symmetric a_1 orbital lies lowest in energy. There are three electrons to fill the orbitals, so that in the ground state two electrons are located in the a_1 orbital, and one in an e orbital. The configuration is then $a_1^2 e^1$, and the spatial symmetry of the many-body wave function in the C_{3v} symmetry induced by the defect is $A_1 \otimes A_1 \otimes E = E$. The $S = 1/2$ spin of the ground state configuration gives a spin doublet, so that the total state corresponds to 2E . As discussed below, this situation is analogous to the configuration of a neutral NV^0 center [63, 64].

A neutral NV^0 center has four molecular orbitals formed from the corresponding dangling bonds, two with a_1 symmetry and a double degenerated e orbital [65]. However, one a_1 orbital is located well below the valence band, and is not relevant for the transitions of interest. The remaining three orbitals are located within the band gap and accommodate three electrons, which is precisely the same configuration as the V_{CF} vacancy in fluorographene. Then, the conclusions derived from group theory for NV centers apply also to V_{CF} . Note that they include the resulting many-body configurations but not necessary their energy order, which is beyond a group theoretical analysis. The similarity motivates also the study of

the negatively charged V_{CF}^- defect, which is analyzed in Section III C.

The many-body configurations corresponding to the ground and first excited states of the V_{CF} defect are presented in Table I. The first excited states are obtained by promoting an electron to the E orbitals, that is, a $a_1^1 e^2$ configuration. The spatial symmetry of the resulting many-body states is given by $A_1 \otimes E \otimes E = A_1 \oplus A_2 \oplus E$. We constructed the electronic configurations given by the single-particle orbitals using the projection operator method. Note that we obtained three doublets with different symmetry and in particular a 2A_2 doublet which, as pointed out in Ref. [64], has been misidentified in some works as 2A_1 for NV^0 . These states can become mixed by different interactions such as spin-orbit, spin-spin, electric and magnetic fields, and strain, as analyzed for NV^0 in several works [64–66].

$2S+1\Gamma_o$	Electronic configuration	Label
2E	$ a_1\bar{a}_1e_x\rangle, a_1\bar{a}_1e_y\rangle$	$\mathcal{E}_{+1/2}^{0(x,y)}$
4A_2	$ a_1e_xe_y\rangle$ $\frac{1}{\sqrt{3}}(\bar{a}_1e_xe_y\rangle + a_1\bar{e}_xe_y\rangle + a_1e_x\bar{e}_y\rangle)$	$\mathcal{A}_{+3/2}^1$ $\mathcal{A}_{+1/2}^1$
${}^2E'$	$\frac{1}{\sqrt{2}}(a_1e_x\bar{e}_x\rangle - a_1e_y\bar{e}_y\rangle)$ $\frac{1}{\sqrt{2}}(a_1e_x\bar{e}_y\rangle - a_1\bar{e}_xe_y\rangle)$	$\mathcal{E}_{+1/2}^{2(x,y)}$
2A_2	$\frac{1}{\sqrt{6}}(2 \bar{a}_1e_xe_y\rangle - a_1\bar{e}_xe_y\rangle - a_1e_x\bar{e}_y\rangle)$	$\mathcal{A}_{+1/2}^3$
2A_1	$\frac{1}{\sqrt{2}}(a_1e_x\bar{e}_x\rangle + a_1e_y\bar{e}_y\rangle)$	$\mathcal{A}_{+1/2}^4$

TABLE I. Electronic configurations of the V_{CF} defect. The notation ${}^2E'$ is used to differentiate this state from the ground state with same symmetry. We label with \mathcal{A} the state with A_1 symmetry, to distinguish it from the states with A_2 symmetry, labeled with \mathcal{A} . We show only the configurations with non-negative spin projections, the ones with negative spin projection can be constructed straightforwardly.

Given that the many-body ground state presents spatial degeneracy, the system is Jahn-Teller unstable, giving rise to an adiabatic potential energy surface (APES) with the typical “Mexican hat” shape [67]. Therefore, the geometrical configuration of the ground state will have a symmetry lower than C_{3v} , namely C_{1h} . For simplicity, we keep the labels of the C_{3v} symmetry for the configurations in our notation. In our analysis, we first relaxed the system while enforcing C_{3v} symmetry to obtain the high symmetry (HS) structure. We then lifted the symmetry restriction and obtained the C_{1h} lower symmetry structure with the lowest energy (LE), a method similar to the one presented in Ref. [68] for the study of a neutral NV^0 center, analogous to our system. For these calculations we used a stricter force convergence criterion of 1 meV/Å.

We found that the Jahn-Teller stabilization energy, which is the energy difference between the HS and LE structures, was $E_{JT} = 30$ meV. This value is about one third of the value found for a neutral NV^0 center [65] and close to the one found for a negatively charged NV^- center [69]. There are three equivalent LE points separated by warping barriers, with saddle points with an energy δ above the minimum [67]. By computing the direct path between two equivalent mini-

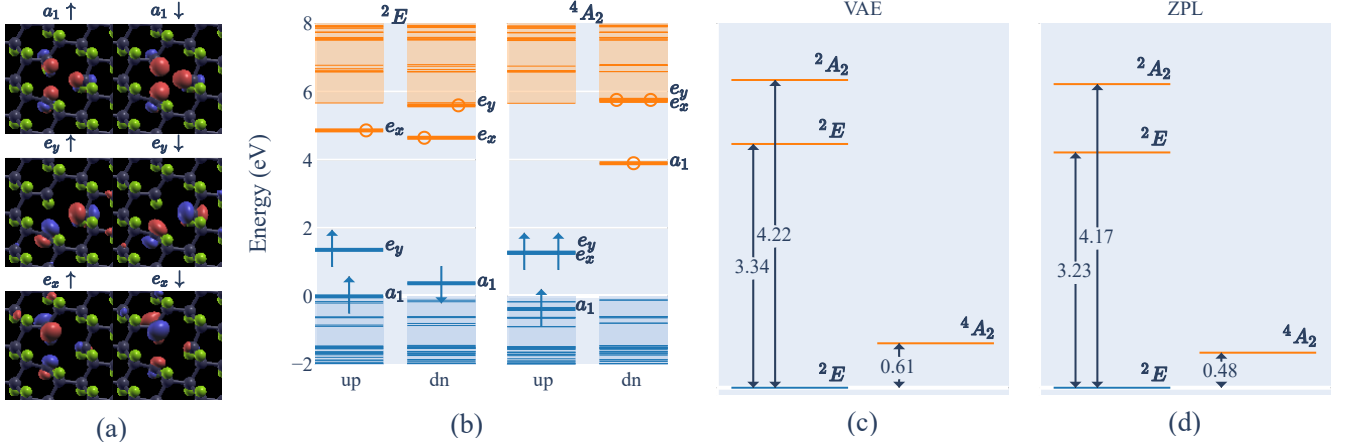


FIG. 2. (a) Geometry of fluorographene with a V_{CF} defect and the resulting localized orbitals. (b) Single-particle levels for the ground state (2E) and first excited state (4A_2) for the V_{CF} defect. The occupied and empty single-electron states are indicated with blue and orange, respectively, and the shaded areas represent the conduction and valence bands. The localized orbitals are labeled and their occupancy is indicated with symbols: empty (circle) or occupied (up or down arrows). (c)-(d) Vertical absorption energy (VAE) and zero-phonon line (ZPL) transitions of the many-body states referred to the ground state, in eV. The 4A_2 state is computed using the Δ SCF method, while the remaining states are computed from auxiliary configurations and should be taken as estimations (see text). Optical transitions are possible among the states in the left side of each plot, while only non-radiative transitions involve the 4A_2 state, located in the right side of the plot.

imum energy configurations located at different LS points, we obtained $\delta = 20$ meV.

In Fig. 2(b) we present the single-particle levels for both the ground state 2E and the first excited state 4A_2 . The levels $\mathcal{E}_{\pm 1/2}^0$ and $\mathcal{A}_{\pm 3/2}^1$ of each manifold can be described by using a single Slater determinant (see Table I). Therefore, the transition energies can be obtained straightforwardly using the Δ SCF method, and are given by the difference between the energies of each configuration. We estimated the transition energies for the remaining excited states using single Slater determinant configurations [55–57] (see Appendix A). While this method has been successfully used to compute transition energies between multi-determinantal configurations, it only provides a rough estimation of the energies [57]. For example, the method does not account accurately for the geometrical relaxation energy (Stokes shift), given that the geometry of the actual configuration cannot be computed. In our calculations of the ZPL for the higher excited states we considered the same geometry as the one obtained for the first excited state, given that all these excited states have the same $a_1^1 e^2$ electronic occupation [56]. Note that the excited state ${}^2E'$ will also present Jahn-Teller distortion, however the accuracy of our method is not enough to estimate its E_{JT} .

In Figs. 2(c) and 2(d) we present the many-body states and their corresponding VAE and ZPL transition energies for the V_{CF} defect. The 2A_1 state lies at 7.8 eV and is omitted. The values of the optical transitions from the ground state to the excited states ${}^2E'$ and 2A_2 , although approximated, are consistent with available experimental data that shows absorption features at around 2.9 eV and 4.8 eV in less fluorinated fluorographene, attributed to single V_F vacancies [36]. Only non-radiative transitions are allowed between these states and the 4A_2 state. The latter state is split via spin-spin interaction

into two double-degenerated states, with $M_S = \pm 1/2$ and $M_S = \pm 3/2$ [65]. Since the $M_S = \pm 3/2$ states only couple via very weak non-axial spin-orbit interaction with the ground state, they are long-lived and have been proposed as qubit candidates for NV^0 centers [65].

In Fig. 3 we present the dependence of the ZPL transition energy between the ground state and the first excited state on strain. Strain is defined as the ratio of the lattice deformation (Δl_i) to its initial dimension (l_i), that is, $\epsilon = \Delta l_i / l_i$ with $i = x, y$. When strain is applied in the y direction, we obtain a variation of -8.5 eV/strain for the transition energy, whereas we obtain a lower value of -1.3 eV/strain when strain is applied in the x direction. The value in the y direction is not far from the large 12 eV/strain shift obtained for $V_N N_B$ defects in h-BN sheets [70]. As shown in Fig. 3(b), strain in the x direction affects mainly the e_y single-particle orbital of the ground state 2E , which is occupied by an electron in our DFT calculation. This dependence is consistent with the geometry of the e_y orbital (see Fig. 2(a)). On the other hand, when strain is applied in the y direction in the ground state, the occupied e_y orbital remains almost constant in energy. Finally, in the excited state 4A_2 both e_x and e_y orbitals are occupied, and the energy change when strain is applied in either direction is similar. As a result, when computing the energy difference between the ground and first excited states, there is a larger variation in energy when strain is applied in the y direction. This is because the energy variation of each state with strain in the x direction partially compensates.

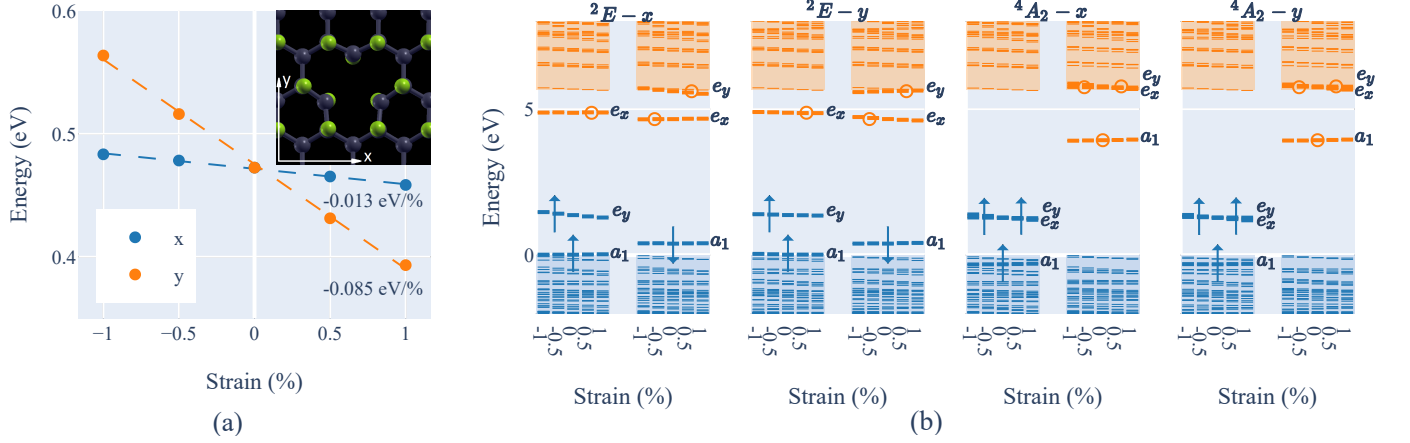


FIG. 3. (a) Strain dependence of the transition energy between the ground state (2E) and the first excited state (4A_2) for a V_{CF}^- defect, for strain applied in the x and y directions (shown in the inset). A linear fit is used to obtain the dependence for each direction. (b) Single-particle levels dependence with strain for each case.

C. V_{CF}^-

As discussed before, the negatively charged V_{CF}^- defect possesses the same symmetry as a NV^- center. In Table II we present the many-body states corresponding to V_{CF}^- , which were obtained using the projection technique of group theory. We adopt the hole picture for the description of this defect, which is more convenient given that the electronic occupation is larger than half-filled. The interactions arising between states have been studied in previous works [71, 72].

$2S+1\Gamma_o$	Electronic configuration	Label
3A_2	$ e_x e_y\rangle$ $\frac{1}{\sqrt{2}}(e_x \bar{e}_y\rangle + \bar{e}_x e_y\rangle)$	$\mathcal{A}_{\pm 1}^0$ \mathcal{A}_0^0
1E	$\frac{1}{\sqrt{2}}(e_x \bar{e}_x\rangle - e_y \bar{e}_y\rangle), \frac{1}{\sqrt{2}}(e_x \bar{e}_y\rangle - e_y \bar{e}_x\rangle)$	$\mathcal{E}_0^{1(x,y)}$
1A_1	$\frac{1}{\sqrt{2}}(e_x \bar{e}_x\rangle + e_y \bar{e}_y\rangle)$	$\tilde{\mathcal{A}}_0^2$
3E	$ a e_x\rangle, a e_y\rangle$ $\frac{1}{\sqrt{2}}(a \bar{e}_x\rangle + \bar{a} e_x\rangle), \frac{1}{\sqrt{2}}(a \bar{e}_y\rangle + \bar{a} e_y\rangle)$	$\mathcal{E}_{\pm 1}^{3(x,y)}$ $\mathcal{E}_0^{3(x,y)}$
${}^1E'$	$\frac{1}{\sqrt{2}}(a \bar{e}_x\rangle - \bar{a} e_x\rangle), \frac{1}{\sqrt{2}}(a \bar{e}_y\rangle - \bar{a} e_y\rangle)$	$\mathcal{E}_0^{4(x,y)}$

TABLE II. Electronic configurations of the V_{CF}^- defect, in the hole picture. The notation ${}^1E'$ is used to differentiate this state from the 1E state with same symmetry. We label with $\tilde{\mathcal{A}}$ the state with A_1 symmetry, to distinguish it from the ground state with A_2 symmetry, labeled with \mathcal{A} . We show only the configurations with non-negative spin projections, the ones with negative spin projection can be constructed straightforwardly.

Only the states $\mathcal{A}_{\pm 1}^0$ and $\mathcal{E}_{\pm 1}^3$ correspond to single-determinant configurations and can be calculated with the Δ SCF method. However, the convergence of the $\mathcal{E}_{\pm 1}^3$ state could not be achieved with the HSE method used. Note that the difficulty in convergence is expected for this case where a hole occupies a degenerated E orbital ($a^1 e_x^1 e_y^2$ electron occu-

pation) [73, 74]. Then, we used the $a^1 e_x^{1.5} e_y^{1.5}$ configuration for the calculation of this state. By comparing the results using the $a^1 e_x^{1.5} e_y^{1.5}$ configuration with preliminary calculations using $a^1 e_x^1 e_y^2$ and a larger convergence threshold, we estimate a difference in the energy of ≈ 0.05 eV, in agreement with previous reports [73].

As in Section III B, we estimated the transition energies of the remaining states by using auxiliary states (see Appendix A). The excited singlets \mathcal{E}_0^1 and \mathcal{A}_0^2 have two holes in the orbitals with E symmetry, which results in the same electronic occupation as the ground state. Then, we considered the ground state geometry in the estimation of the ZPL for these excited states, assuming their ZPL energies equal to their vertical excitation energies. According to Hund's rules, the remaining singlet \mathcal{E}_0^4 lies higher in energy than the excited triplet $\mathcal{E}_{\pm 1}^3$, so that we omitted it.

In Fig. 4(a) we present the single-particle levels for the ground state, which can be described with a single determinant. The empty e orbitals of the ground state 3A_2 are pushed up in energy into the conduction band when compared to the same levels of the 4A_2 state of the neutral V_{CF} defect (Fig. 2(b)). However, our DFT calculations show that these states remain well localized, and the molecular orbitals are similar to those shown in Fig. 2(a).

In Fig. 4(b) we show the VAE transitions for the excited states. As discussed before, the VAE provides an estimation of the ZPL for the singlet states. For the excited triplet 3E we obtained a ZPL energy of 2.3 eV. Note that this value of ZPL for 3E is lower than the absorption features experimentally observed [36–38]. This indicates that the presence of the negatively charged defects is not energetically favored, which is consistent with the formation energy analysis presented in Section III E. Consequently, the negatively charged state should be stabilized by applying a gate voltage.

A distinguishing feature of the NV^- center defect is that it allows for high fidelity preparation of the $m = 0$ sublevel of

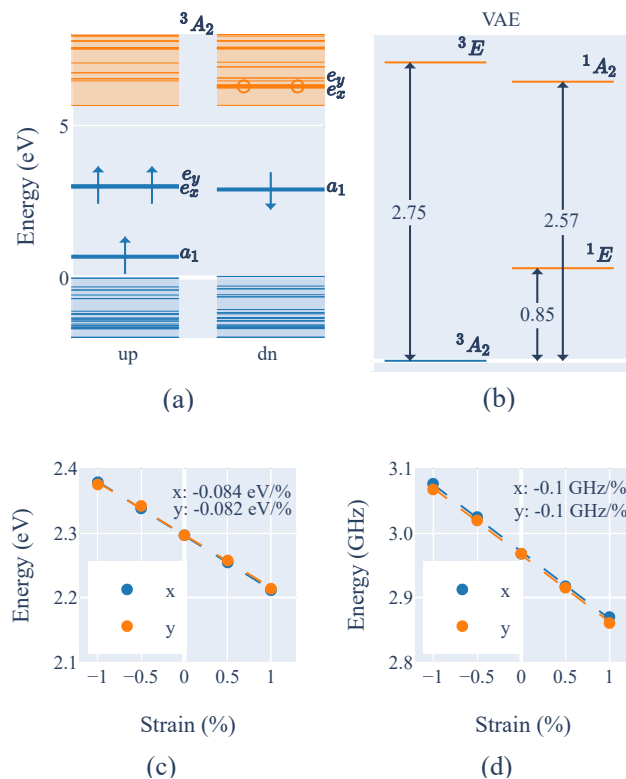


FIG. 4. (a) Single-particle levels for the ground state (3A_2) and the excited state 3E for the V_{CF}^- defect. (b) Vertical absorption energy (VAE) transitions of the many-body states referred to the ground state, in eV. The 3E state is computed using the Δ SCF method, while the remaining states are computed from auxiliary configurations. Optical transitions are possible among states in the left or right side of the plot, while only non-radiative transitions are possible among different sides. The estimated ZPL of 1E and 1A_2 are equal to the VAE. The ZPL of 3E is 2.3 eV. (c) Strain dependence of the transition energy between 3A_2 and 3E , for strain applied in the x and y directions. A linear fit is used to obtain the dependence for each direction. (d) Strain dependence of the ZFS of the 3A_2 triplet.

its ground state, labeled \mathcal{A}_0^0 in our system, due to a convenient intersystem crossing (ISC) between triplet and singlet states [2]. Taking as reference the VAE of the many-body states of V_{CF}^- (Fig. 4(b)), the ordering of the levels for our system would be the same as that of the NV center. If that was indeed the case, symmetry considerations allow in principle the existence of a similar ISC, which could then be tested using available models [75]. However, our rough estimations for the ZPL values suggest that the 1A_2 singlet remains above the 3E triplet. In order to decide this question conclusively it is of considerable interest to extend this study using alternative *ab-initio* methods better suited for the calculation of multireference states [49], since an accurate description of the states ordering is a first step to determine if an ISC similar to the one in NV^- centers is also present in V_{CF}^- defects in FG.

Spin-orbit and spin-spin interactions split the excited states 3E into four sublevels, and the fine structure is further split into two branches (E_x , E_y) under the application of non-axial

strain [72]. Figure 4(c) shows the dependence of the ZPL of the 3E state with application of strain in x and y directions. We obtained a value of approximately -8 eV/strain for both directions which, as in the case of the neutral defect, is comparable to the strain shift obtained for defects in h-BN sheets [70].

Another parameter of interest in the description of the defect is the zero-field splitting (ZFS) tensor. The ZFS is determined to first order by dipolar spin-spin interactions, and we calculated its value for the ground state from our DFT results [76]. For the C_{3v} symmetry of the defect, only the axial ZFS parameter D is different from zero. We obtained $D = 2.97$ GHz, which is close to the value for NV centers ($D = 2.88$ GHz [2]). In addition, we calculated the dependence of the ZFS for the 3A_2 ground state on strain (Fig. 4(d)). We obtained a shift of -10 GHz/strain for both directions. The symmetry breaking induced by strain allows a non-zero value of the transversal component of the ZFS (E parameter). Our calculations yield a value of $E \approx -20$ MHz for $\pm 1\%$ strain, which is close to the numerical accuracy of the method used.

D. Applications to hybrid resonators

Strain induced by the mechanical motion of the material, for example, through the drum oscillatory modes of a FG membrane suspended from its edges, provides an intrinsic mean of coupling phonons with electronic degrees of freedom. This method does not require the use of external components, resulting in a device that is less prone to noise and decoherence, and has lower complexity in its scalability than devices relying on auxiliary components to provide the coupling [4]. However, intrinsic strain coupling is typically relatively small, which led to several proposals aimed at increasing the interaction by using electric or magnetic fields [23], or cavities [4] coupled to the resonator.

Depending on the system, qubits can be encoded in either the orbital or spin electronic degrees of freedom of color centers, which makes orbit-strain or spin-strain interactions relevant for phonon coupling [4]. Typically, the spin-strain coupling strength is rather small, with values in the order of 10 GHz/strain for devices with implanted NV centers [77, 78]. On the other hand, orbit-strain coupling is much stronger, approximately 10^8 times larger than spin-strain coupling, given that the molecular orbitals are directly affected by the changes in the lattice induced by mechanical motion [79]. Values for orbit-strain coupling are typically in the range of PHz/strain for different quantum hybrid devices using NV centers [79] and h-BN sheets with defects [70, 80, 81].

The dynamics of a freestanding 2D material sheet can be described through the elasticity theory of membranes. In the membrane limit in which the material has vanishing thickness, which is fulfilled by single or few layers sheets, the frequency of the fundamental mechanical mode ω_m^0 for membranes with simple geometries is approximated in terms of the pretension T , the surface mass density ρ_s , a geometrical form factor α given by the non-trivial zero of the mode profile and a charac-

teristic dimension of the system d [17, 82, 83],

$$\omega_m^0 = \frac{\alpha}{d} \sqrt{\frac{T}{\rho_s}}. \quad (4)$$

For a circular membrane, $\alpha = 2.4$ and d is equal to the radius R [82, 84], while for a ribbon of length L clamped in the extremes, $\alpha = \pi$ and $d = L$ [80]. The pretension value depends on the fabrication of the membrane [60], and is related to the strain ϵ and in-plane Young's module of the material E_s by $T = E_s \epsilon$. For graphene membranes of a few μm of radius, T was estimated to be $\approx 4 \times 10^{-2}$ N/m [85]. For fluorographene, $\rho_s = 1.706$ mg/m² [60] and $E_s = 100$ N/m [31]. Taking $T \approx 4 \times 10^{-2}$ N/m as reference, we obtain $\omega_m^0 \approx 10$ MHz for fluorographene membranes of $d \approx 1$ μm , a value in agreement with the ones obtained for similar devices of h-BN [23] and graphene [17, 19, 83, 85]. It is worth mentioning that driven devices can achieve frequencies of the order of GHz, as was obtained for MoS₂ piezo-resonators [20].

The membrane strain is related to its deflection, and for small deflections it can be approximately written in terms of the maximum vertical displacement ξ [85],

$$\epsilon = \beta \left(\frac{\xi}{d} \right)^2, \quad (5)$$

where β is a geometrical factor, which for a ribbon-shaped membrane corresponds to $8/3$ [85]. Static deflections in membrane devices can be tuned using a voltage gate, and typical values for membranes of a few μm of radius are in the order of 10 nm, that leads to static built-in strains of $\approx 10^{-4}$ [85]. Strain induced dynamically through time-dependent bias can achieve the same order of magnitude [85]. The fundamental oscillation modes of micro-scale membranes around the equilibrium point have a vertical displacement of approximately 0.1 nm, which corresponds to an induced strain of $\epsilon \approx 10^{-8}$. These reference values correspond to a h-BN ribbon [80]. The quadratic dependence of the strain with the vertical displacement, which in turn depends on the membrane geometry and material through $\xi = \sqrt{\hbar/(2M\omega_m^0)}$ (M is the effective mass) [23, 80], leads to a spread in the reference values, ranging from $\xi \approx 10^{-2}$ nm and $\epsilon \approx 10^{-10}$ for a similar h-BN device [23] to $\xi \approx 10$ nm and $\epsilon \approx 10^{-4}$ for the already mentioned driven resonators [85]. For comparison, the strain of a three-dimensional (3D) diamond micro cantilever with implanted NV centers in the fundamental mode is $\approx 10^{-12}$, and can be increased to $\approx 10^{-6}$ through mechanical drive [79]. A scaling-down of the latter device to the nanoscale was proposed to achieve a larger orbit-strain coupling (up to the ≈ 10 MHz) in the fundamental mode [79], through a larger induced strain. In this regard, 2D membranes arise as promising candidates, given their comparatively large achievable strain.

Our *ab-initio* calculations suggest a deformation potential [22] of $\Xi \approx 1$ PHz/strain for fluorographene membranes, a value similar to the one obtained for previously studied h-BN resonators [22, 80]. If we consider a fluorographene membrane of $d \approx 1$ μm hosting a color center and oscillating in the fundamental mode with a vertical displacement of $\xi \approx 0.1$ nm, we obtain an orbit-strain coupling of $g = 10$ MHz.

The obtained coupling is about 10^3 times larger than the values obtained for 3D mechanical resonators with NV⁻ centers [4, 79]. For the latter devices, different cooling schemes were proposed [4, 5, 86]. The ‘‘off-resonant’’ scheme uses the $m_s = 0$ sublevel \mathcal{A}_0^0 of the ground state and the \mathcal{E}_0^{3y} level of 3E as two-level system, and convert the strain coupling to an effective transverse interaction using a laser detuned by ω_m^0 from the transition energy [4]. The ‘‘resonant’’ scheme involves tuning the energy difference between the \mathcal{E}_0^{3x} and \mathcal{E}_0^{3y} levels of the 3E state to be equal to ω_m^0 , while driving the transition from the \mathcal{A}_0^0 ground state to \mathcal{E}_0^{3y} with a laser. This allows for resonant excitation to the \mathcal{E}_0^{3x} state by removing a phonon from the mechanical mode [4]. However, scaling down these devices from the microscale to the nanoscale is necessary to achieve ground-state cooling using these methods [4, 79]. The inherent larger coupling in our system would enable the implementation of these methods in a fluorographene membrane device, thereby extending the proposal for the NV⁻ center to the V_{CF} defect. Another possible protocol uses the $\mathcal{A}_{\pm 1}^0$ levels in a Λ configuration with an excited state formed with the $\mathcal{E}_{\pm 1}^{3(x,y)}$ levels, which are mixed through spin-orbit interaction [72]. This scheme relies on stimulated Raman transitions to remove phonons from the resonator, and has the advantage of combining the stronger orbit-strain coupling with the larger coherence of spin states [4].

E. Formation energy and stability

The formation energy for a defect with charge q is obtained from [87]

$$E_f^q(\epsilon_F) = E_d^q - E_{\text{bulk}} - \sum_i n_i \mu_i + q\epsilon_F + E_{\text{corr}}^q, \quad (6)$$

where E_d^q is the total energy of the supercell with the defect, E_{bulk} is the energy of the pristine supercell, n_i are the number of atoms that have been added ($n_i > 0$) or removed ($n_i < 0$) to form the defect, with μ_i the corresponding chemical potentials. The energy depends on the total charge with the Fermi energy ϵ_F , measured from the top of the valence band. The final term E_{corr}^q accounts for corrections such as finite k-point sampling and electrostatic interactions [87, 88]. Here, we apply the Freysoldt–Neugebauer–Van de Walle (FNV) correction scheme [89, 90].

In Fig. 5 we present the formation energy for the V_F and V_{CF} defects as a function of the Fermi energy, which can be varied by applying a gate voltage. We considered two different scenarios for the chemical potentials. In the first scenario, the defective membrane is in equilibrium with F_2 , which results in a fluorine-rich environment. For this case, we obtain $\mu_F = \mu_{F_2}/2$ from the energy of a F_2 molecule and $\mu_C = \mu_{\text{FG}} - \mu_F$ from the difference between the energy of the pristine fluorographene primitive cell (μ_{FG}) and the fluorine chemical potential. In the second scenario, we considered a carbon-rich environment and calculated μ_C from a graphene primitive cell. We obtained the fluorine chemical potential from the difference with μ_{FG} , which gives $\mu_F = \mu_{\text{FG}} - \mu_C$.

The formation energy of V_{CF} is independent from the environment, since the third term in Eq. (6), $\sum_i n_i \mu_i = n_C \mu_C + n_F \mu_F$, equals μ_{FG} by definition for both environments. On the other hand, the formation energy for the V_F defect is higher in the F_2 -rich environment, as expected. The formation energy of V_F is higher than that of V_{CF} only in the special condition of F_2 -rich environment and $\epsilon_F \lesssim -0.5$ eV. For the remaining conditions, the V_F defect is more stable than V_{CF} . However, molecular dynamics calculations suggest that the latter defect is also thermodynamically stable [47].

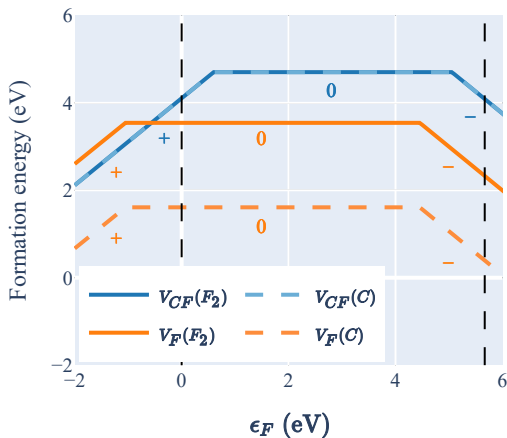


FIG. 5. Formation energy as a function of the Fermi energy for V_F and V_{CF} defects, for F_2 -rich and C-rich environments. The black dashed lines indicate the position of the top of the valence and the bottom of the conduction bands. The favorable charge states (+, 0 or -) of the defects are also indicated.

IV. CONCLUSIONS

In this study, we investigated the electronic properties of V_F , V_{CF} and V_{CF}^- defects in FG membranes. We computed the many-body states from single-particle DFT results making use of group-theoretical considerations, obtained the transition energies between the states and analyzed their dependence with non-axial strain. The obtained energy shift under strain for the studied defects was in the order of 1 PHz/strain, which is comparable to the one found for defects in h-BN sheets. This value leads to an orbit-strain coupling of $g \approx 10$ MHz for membranes of $\approx 1 \mu\text{m}$. Due to the similarities of V_{CF} defects in FG with NV centers on diamond, some proposals for NV centers resonators can be mapped to 2D devices based on FG with V_{CF}^- defects, taking advantage of the larger strain achievable in 2D materials. Furthermore, extending this study with alternative *ab-initio* methods would be useful to deter-

mine if an ISC similar to the one present in NV centers could also be expected in this system. Our findings suggest that the V_{CF} defect in FG membranes can be a promising candidate for developing nanomechanical resonators with strong orbit-strain coupling and contribute to the understanding of defects in two-dimensional materials and their quantum applications.

ACKNOWLEDGMENTS

This work was supported by the ERC Synergy grant Hy-sterQ (Grant No. 856432) and by the BMBF via the project CoGeQ (grant No. 13N16101). The authors acknowledge support by the state of Baden-Württemberg through bwHPC and the German Research Foundation (DFG) through grant No. INST 40/575-1 FUGG (JUSTUS 2 cluster). M. S. T. thanks J. S. Pedernales for helpful discussions.

Appendix A: Multi-configurational States

For V_{CF} , the ground and first excited states are directly described by a single determinant, while the remaining states are multi-configurational. In principle, the Δ SCF method does not allow to compute configurations composed by several determinants. However, it is possible to obtain a rough estimation of these multi-configurational states from single-determinant auxiliary configurations [55, 56]. To illustrate the method, consider the state \mathcal{A}^3 . We note that

$$\sqrt{2}\mathcal{A}_{+1/2}^3 + \mathcal{A}_{+1/2}^1 = \sqrt{3}|\bar{a}_1 e_x e_y\rangle. \quad (\text{A1})$$

Considering that the energy of the states is independent of the spin projection, $E(\mathcal{A}_{+1/2}^1) = E(\mathcal{A}_{+3/2}^1) = E(\mathcal{A}^1)$, we obtain

$$E(\mathcal{A}^3) = \frac{1}{2}(3E(|\bar{a}_1 e_x e_y\rangle) - E(\mathcal{A}^1)). \quad (\text{A2})$$

Similarly, for the two remaining excited states of V_{CF} we obtain the following expressions,

$$E(\mathcal{E}^2) = \frac{1}{3}(6E(|a_1 e_x \bar{e}_y\rangle) - 2E(\mathcal{A}^1) - E(\mathcal{A}^3)) \quad (\text{A3})$$

$$E(\mathcal{A}^4) = 2E(|a_1 e_x \bar{e}_x\rangle) - E(\mathcal{E}^2). \quad (\text{A4})$$

For V_{CF}^- , we obtain the following expressions for the transition energies of the multiconfigurational states

$$E(\mathcal{E}^1) = 2E(|e_x \bar{e}_y\rangle) \quad (\text{A5})$$

$$E(\mathcal{A}'^2) = 2E(|e_x \bar{e}_x\rangle) - E(\mathcal{E}^1) \quad (\text{A6})$$

$$E(\mathcal{E}^4) = 2E(|a \bar{e}_x\rangle). \quad (\text{A7})$$

[1] J. Wrachtrup and F. Jelezko, Processing quantum information in diamond, *Journal of Physics: Condensed Matter* **18**, 0807

(2006).

[2] M. W. Doherty, N. B. Manson, P. Delaney, F. Jelezko,

- J. Wrachtrup, and L. C. Hollenberg, The nitrogen-vacancy colour centre in diamond, *Physics Reports* **528**, 1 (2013).
- [3] Y. Wu, F. Jelezko, M. B. Plenio, and T. Weil, Diamond Quantum Devices in Biology, *Angewandte Chemie International Edition* **55**, 6586 (2016).
- [4] D. Lee, K. W. Lee, J. V. Cady, P. Ovartchayapong, and A. C. Jayich, Topical review: Spins and mechanics in diamond, *Journal of Optics* **19**, 033001 (2017).
- [5] K. V. Kepesidis, S. D. Bennett, S. Portolan, M. D. Lukin, and P. Rabl, Phonon cooling and lasing with nitrogen-vacancy centers in diamond, *Physical Review B* **88**, 064105 (2013).
- [6] T. Ramos, V. Sudhir, K. Stannigel, P. Zoller, and T. J. Kippenberg, Nonlinear quantum optomechanics via individual intrinsic two-level defects, *Physical Review Letters* **110**, 193602 (2013).
- [7] S. D. Bennett, N. Y. Yao, J. Otterbach, P. Zoller, P. Rabl, and M. D. Lukin, Phonon-induced spin-spin interactions in diamond nanostructures: Application to spin squeezing, *Physical Review Letters* **110**, 156402 (2013).
- [8] D. A. Golter, T. Oo, M. Amezcua, K. A. Stewart, and H. Wang, Optomechanical Quantum Control of a Nitrogen-Vacancy Center in Diamond, *Physical Review Letters* **116**, 143602 (2016).
- [9] R. J. Dolleman, S. Hourii, A. Chandrashekar, F. Alijani, and H. S. J. Van, Opto-thermally excited multimode parametric resonance in graphene membranes, *Scientific Reports* **8**, 9366 (2018).
- [10] P. G. Steeneken, R. J. Dolleman, D. Davidovikj, F. Alijani, and H. S. Van Der Zant, Dynamics of 2D material membranes, *2D Materials* **8**, 042001 (2021).
- [11] A. Pokharel, H. Xu, S. Venkatachalam, E. Collin, and X. Zhou, Coupling Capacitively Distinct Mechanical Resonators for Room-Temperature Phonon-Cavity Electromechanics, *Nano Letters* **22**, 7351 (2022).
- [12] M. J. Burek, N. P. De Leon, B. J. Shields, B. J. Hausmann, Y. Chu, Q. Quan, A. S. Zibrov, H. Park, M. D. Lukin, and M. Lončar, Free-standing mechanical and photonic nanostructures in single-crystal diamond, *Nano Letters* **12**, 6084 (2012).
- [13] J. Chan, T. P. Alegre, A. H. Safavi-Naeini, J. T. Hill, A. Krause, S. Gröblacher, M. Aspelmeyer, and O. Painter, Laser cooling of a nanomechanical oscillator into its quantum ground state, *Nature* **478**, 89 (2011).
- [14] M. Hoese, P. Reddy, A. Dietrich, M. K. Koch, K. G. Fehler, M. W. Doherty, and A. Kubanek, Mechanical decoupling of quantum emitters in hexagonal boron nitride from low-energy phonon modes, *Science Advances* **6**, eaba6038 (2020).
- [15] M. Abdi, J. P. Chou, A. Gali, and M. B. Plenio, Color Centers in Hexagonal Boron Nitride Monolayers: A Group Theory and Ab Initio Analysis, *ACS Photonics* **5**, 1967 (2018).
- [16] R. Fandan, J. Pedrós, A. Hernández-Mínguez, F. Iikawa, P. V. Santos, A. Boscá, and F. Calle, Dynamic Local Strain in Graphene Generated by Surface Acoustic Waves, *Nano Letters* **20**, 402 (2020).
- [17] R. A. Barton, B. Ilic, A. M. Van Der Zande, W. S. Whitney, P. L. McEuen, J. M. Parpia, and H. G. Craighead, High, size-dependent quality factor in an array of graphene mechanical resonators, *Nano Letters* **11**, 1232 (2011).
- [18] R. De Alba, F. Massel, I. R. Storch, T. S. Abhilash, A. Hui, P. L. McEuen, H. G. Craighead, and J. M. Parpia, Tunable phonon-cavity coupling in graphene membranes, *Nature Nanotechnology* **11**, 741 (2016).
- [19] G. J. Verbiest, M. Goldsche, J. Sonntag, T. Khodkov, N. von den Driesch, D. Buca, and C. Stampfer, Tunable coupling of two mechanical resonators by a graphene membrane, *2D Materials* **8**, 035039 (2021).
- [20] C. Jiang, Q. Li, J. Huang, S. Bi, R. Ji, and Q. Guo, Single-Layer MoS₂ Mechanical Resonant Piezo-Sensors with High Mass Sensitivity, *ACS Appl. Mater. Interfaces* **12**, 41991 (2020).
- [21] A. Castellanos-Gomez, R. Van Leeuwen, M. Buscema, H. S. Van Der Zant, G. A. Steele, and W. J. Venstra, Single-layer MoS₂ mechanical resonators, *Advanced Materials* **25**, 6719 (2013).
- [22] S. Li, J. P. Chou, A. Hu, M. B. Plenio, P. Udvarhelyi, G. Thiering, M. Abdi, and A. Gali, Giant shift upon strain on the fluorescence spectrum of VNNB color centers in h-BN, *npj Quantum Information* **6**, 85 (2020).
- [23] M. Abdi, M. J. Hwang, M. Aghtar, and M. B. Plenio, Spin-Mechanical Scheme with Color Centers in Hexagonal Boron Nitride Membranes, *Physical Review Letters* **119**, 233602 (2017).
- [24] A. Castellanos-Gomez, V. Singh, H. S. Van Der Zant, and G. A. Steele, Mechanics of freely-suspended ultrathin layered materials, *Annalen der Physik* **527**, 27 (2015).
- [25] E. Blundo, E. Cappelluti, M. Felici, G. Pettinari, and A. Polimeni, Strain-tuning of the electronic, optical, and vibrational properties of two-dimensional crystals, *Applied Physics Reviews* **8**, 021318 (2021).
- [26] T. T. Tran, K. Bray, M. J. Ford, M. Toth, and I. Aharonovich, Quantum emission from hexagonal boron nitride monolayers, *Nat. Nanotechnol.* **11**, 37 (2016).
- [27] S. Vaidya, X. Gao, S. Dikshit, I. Aharonovich, and T. Li, Quantum sensing and imaging with spin defects in hexagonal boron nitride, *Advances in Physics: X* **8**, 2206049 (2023).
- [28] M. Abdi and M. B. Plenio, Analog quantum simulation of extremely sub-ohmic spin-boson models, *Phys. Rev. A* **98**, 040303 (2018).
- [29] R. Gong, G. He, X. Gao, P. Ju, Z. Liu, B. Ye, E. A. Henriksen, T. Li, and C. Zu, Coherent dynamics of strongly interacting electronic spin defects in hexagonal boron nitride, *Nature Communications* **14**, 3299 (2023).
- [30] R. Zbořil, F. Karlický, A. B. Bourlinos, T. A. Steriotis, A. K. Stubos, V. Georgakilas, K. Šafařová, D. Jančík, C. Trapalis, and M. Otyepka, Graphene fluoride: A stable stoichiometric graphene derivative and its chemical conversion to graphene, *Small* **6**, 2885 (2010).
- [31] R. R. Nair, Fluorographene: A Two-Dimensional Counterpart of Teflon, *Small* **6**, 2877 (2010).
- [32] D. D. Chronopoulos, A. Bakandritsos, M. Pykal, R. Zbořil, and M. Otyepka, Chemistry, properties, and applications of fluorographene, *Applied Materials Today* **9**, 60 (2017).
- [33] J. Cai, A. Retzker, F. Jelezko, and M. B. Plenio, A large-scale quantum simulator on a diamond surface at room temperature, *Nature Physics* **9**, 168 (2013).
- [34] X. Gao, S. Vaidya, K. Li, P. Ju, B. Jiang, Z. Xu, A. E. Allcca, K. Shen, T. Taniguchi, K. Watanabe, S. A. Bhave, Y. P. Chen, Y. Ping, and T. Li, Nuclear spin polarization and control in hexagonal boron nitride, *Nature Materials* **21**, 1024 (2022).
- [35] F. T. Tabesh, M. Fani, J. S. Pedernales, M. B. Plenio, and M. Abdi, Active hyperpolarization of the nuclear spin lattice: Application to hexagonal boron nitride color centers, *Phys. Rev. B* **107**, 214307 (2023).
- [36] V. Hrubý, L. Zdražil, J. Džíbelová, V. Šedajová, A. Bakandritsos, P. Lazar, and M. Otyepka, Unveiling the true band gap of fluorographene and its origins by teaming theory and experiment, *Applied Surface Science* **587**, 152839 (2022).
- [37] K. J. Jeon, Z. Lee, E. Pollak, L. Moreschini, A. Bostwick, C. M. Park, R. Mendelsberg, V. Radmilovic, R. Kosteckí, T. J. Richardson, and E. Rotenberg, Fluorographene: A wide bandgap semiconductor with ultraviolet luminescence, *ACS Nano* **5**, 1042 (2011).

- [38] V. Mazánek, O. Jankovský, J. Luxa, D. Sedmidubský, Z. Janoušek, F. Šembera, M. Mikulics, and Z. Sofer, Tuning of fluorine content in graphene: towards large-scale production of stoichiometric fluorographene, *Nanoscale* **7**, 13646 (2015).
- [39] P. Hohenberg and W. Kohn, Inhomogeneous Electron Gas, *Physical Review* **136**, 864 (1964).
- [40] J. Zhou, Q. Liang, and J. Dong, Enhanced spin-orbit coupling in hydrogenated and fluorinated graphene, *Carbon* **48**, 1405 (2010).
- [41] M. Klintonberg, S. Lebègue, M. I. Katsnelson, and O. Eriksson, Theoretical analysis of the chemical bonding and electronic structure of graphene interacting with Group IA and Group VIIA elements, *Physical Review B* **81**, 085433 (2010).
- [42] O. Leenaerts, H. Peelaers, A. D. Hernández-Nieves, B. Partoens, and F. M. Peeters, First-principles investigation of graphene fluoride and graphane, *Physical Review B* **82**, 195436 (2010).
- [43] F. Karlický, R. Zbořil, and M. Otyepka, Band gaps and structural properties of graphene halides and their derivatives: A hybrid functional study with localized orbital basis sets, *J. Chem. Phys.* **137**, 034709 (2012).
- [44] D. K. Samarakoon, Z. Chen, C. Nicolas, and X. Q. Wang, Structural and electronic properties of fluorographene, *Small* **7**, 965 (2011).
- [45] F. Karlický and M. Otyepka, Band gaps and optical spectra of chlorographene, fluorographene and graphane from G0W0, GW0 and GW calculations on top of PBE and HSE06 orbitals, *J. Chem. Theory Comput.* **9**, 4155 (2013).
- [46] W. Wei and T. Jacob, Electronic and optical properties of fluorinated graphene: A many-body perturbation theory study, *Physical Review B* **87**, 115431 (2013).
- [47] D. Li, X. Ma, H. Chu, Y. Li, S. Zhao, and D. Li, Vacancy-induced magnetism in fluorographene: The effect of midgap state, *Molecules* **26**, 6666 (2021).
- [48] S. A. Tawfik, S. Ali, M. Fronzi, M. Kianinia, T. T. Tran, C. Stampfl, I. Aharonovich, M. Toth, and M. J. Ford, First-principles investigation of quantum emission from hBN defects, *Nanoscale* **9**, 13575 (2017).
- [49] J. R. Reimers, A. Sajid, R. Kobayashi, and M. J. Ford, Understanding and Calibrating Density-Functional-Theory Calculations Describing the Energy and Spectroscopy of Defect Sites in Hexagonal Boron Nitride, *Journal of Chemical Theory and Computation* **14**, 1602 (2018).
- [50] P. Giannozzi, S. Baroni, N. Bonini, M. Calandra, R. Car, C. Cavazzoni, D. Ceresoli, G. L. Chiarotti, M. Cococcioni, I. Dabo, A. D. Corso, S. D. Gironcoli, S. Fabris, G. Fratesi, R. Gebauer, U. Gerstmann, C. Gougoussis, A. Kokalj, M. Lazzeri, L. Martin-samos, N. Marzari, F. Mauri, R. Mazzarello, S. Paolini, A. Pasquarello, L. Paulatto, C. Sbraccia, A. Smogunov, and P. Umari, QUANTUM ESPRESSO: a modular and open-source software project for quantum simulations of materials, *J. Phys.: Condens. Matter* **21**, 395502 (2009).
- [51] J. P. Perdew, K. Burke, and M. Ernzerhof, Generalized gradient approximation made simple, *Phys. Rev. Lett.* **77**, 3865 (1996).
- [52] J. Perdew, K. Burke, and M. Ernzerhof, Generalized gradient approximation made simple [Phys. Rev. Lett. 77, 3865 (1996)], *Phys. Rev. Lett.* **78**, 1396 (1997).
- [53] R. Jones and O. Gunnarsson, The density functional formalism, its applications and prospects, *Reviews of Modern Physics* **61**, 689 (1989).
- [54] B. R. A. Hellman and B. I. Lundqvist, Potential-energy surfaces for excited states in extended systems, *J. Chem. Phys.* **120**, 4593 (2004).
- [55] O. Golami, K. Sharman, R. Ghobadi, S. C. Wein, H. Zadeh-Haghighi, C. Gomes da Rocha, D. R. Salahub, and C. Simon, Ab initio and group theoretical study of properties of a carbon trimer defect in hexagonal boron nitride, *Physical Review B* **105**, 184101 (2022).
- [56] M. MacKoit-Sinkevičiene, M. MacIaszek, C. G. Van De Walle, and A. Alkauskas, Carbon dimer defect as a source of the 4.1 eV luminescence in hexagonal boron nitride, *Applied Physics Letters* **115**, 212101 (2019).
- [57] A. Gali, M. Fyta, and E. Kaxiras, Ab initio supercell calculations on nitrogen-vacancy center in diamond: Electronic structure and hyperfine tensors, *Physical Review B* **77**, 155206 (2008).
- [58] G. Thiering and A. Gali, Ab initio calculation of spin-orbit coupling for an NV center in diamond exhibiting dynamic Jahn-Teller effect, *Physical Review B* **96**, 081115 (2017).
- [59] A. Markevich, R. Jones, and P. R. Briddon, Doping of fluorographene by surface adsorbates, *Physical Review B* **84**, 115439 (2011).
- [60] M. E. Belenkov, V. M. Chernov, and E. A. Belenkov, Structure of fluorographene and its polymorphous varieties, *J. Phys.: Conf. Ser.* **1124**, 022010 (2018).
- [61] S. H. Cheng, K. Zou, F. Okino, H. R. Gutierrez, A. Gupta, N. Shen, P. C. Eklund, J. O. Sofo, and J. Zhu, Reversible fluorination of graphene: Evidence of a two-dimensional wide bandgap semiconductor, *Physical Review B* **81**, 205435 (2010).
- [62] M. Tinkham, *Group Theory and Quantum Mechanics* (Courier Corporation, 2003).
- [63] S. Felton, A. M. Edmonds, M. E. Newton, P. M. Martineau, D. Fisher, and D. J. Twitchen, Electron paramagnetic resonance studies of the neutral nitrogen vacancy in diamond, *Physical Review B* **77**, 081201(R) (2008).
- [64] N. B. Manson, K. Beha, A. Batalov, L. J. Rogers, M. W. Doherty, R. Bratschitsch, and A. Leitenstorfer, Assignment of the NV⁰ 575-nm zero-phonon line in diamond to a ²E - ²A₂ transition, *Physical Review B* **87**, 155209 (2013).
- [65] A. Gali, Theory of the neutral nitrogen-vacancy center in diamond and its application to the realization of a qubit, *Physical Review B* **79**, 235210 (2009).
- [66] M. S. Barson, E. Krausz, N. B. Manson, and M. W. Doherty, The fine structure of the neutral nitrogen-vacancy center in diamond, *Nanophotonics* **8**, 1985 (2019).
- [67] I. B. Bersuker, *The Jahn Teller effect* (Cambridge University Press, 2009).
- [68] J. Zhang, C. Z. Wang, Z. Zhu, Q. H. Liu, and K. M. Ho, Multimode Jahn-Teller effect in bulk systems: A case of the NV⁰ center in diamond, *Physical Review B* **97**, 165204 (2018).
- [69] Á. Gali, Ab initio theory of the nitrogen-vacancy center in diamond, *Nanophotonics* **8**, 1907 (2019).
- [70] M. Abdi and M. B. Plenio, Quantum Effects in a Mechanically Modulated Single-Photon Emitter, *Physical Review Letters* **122**, 23602 (2019).
- [71] J. R. Maze, A. Gali, E. Togan, Y. Chu, A. Trifonov, E. Kaxiras, and M. D. Lukin, Properties of nitrogen-vacancy centers in diamond: The group theoretic approach, *New Journal of Physics* **13**, 025025 (2011).
- [72] M. W. Doherty, N. B. Manson, P. Delaney, and L. C. Hollenberg, The negatively charged nitrogen-vacancy centre in diamond: The electronic solution, *New Journal of Physics* **13**, 025019 (2011).
- [73] Y. Jin, M. Govoni, G. Wolfowicz, S. E. Sullivan, F. J. Heremans, D. D. Awschalom, and G. Galli, Photoluminescence spectra of point defects in semiconductors: Validation of first-principles calculations, *Physical Review Materials* **5**, 084603 (2021).
- [74] J. Gavnholt, T. Olsen, M. Englund, and J. Schiøtz, Δ Self-

- Consistent Field Method To Obtain Potential Energy Surfaces of Excited Molecules on Surfaces, *Physical Review B* **78**, 075441 (2008).
- [75] M. L. Goldman, M. W. Doherty, A. Sipahigil, N. Y. Yao, S. D. Bennett, N. B. Manson, A. Kubanek, and M. D. Lukin, State-selective intersystem crossing in nitrogen-vacancy centers, *Physical Review B* **91**, 165201 (2015).
- [76] H. Ma, M. Govoni, and G. Galli, PyZFS: A Python package for first-principles calculations of zero-field splitting tensors, *Journal of Open Source Software* **5**, 2160 (2020).
- [77] P. Ouartchaiyapong, K. W. Lee, B. A. Myers, and A. C. B. Jayich, Dynamic strain-mediated coupling of a single diamond spin to a mechanical resonator, *Nature Communications* **5**, 4429 (2014).
- [78] J. Teissier, A. Barfuss, P. Appel, E. Neu, and P. Maletinsky, Strain Coupling of a Nitrogen-Vacancy Center Spin to a Diamond Mechanical Oscillator, *Physical Review Letters* **113**, 020503 (2014).
- [79] K. W. Lee, D. Lee, P. Ouartchaiyapong, J. Minguzzi, J. R. Maze, and A. C. Bleszynski Jayich, Strain Coupling of a Mechanical Resonator to a Single Quantum Emitter in Diamond, *Physical Review Applied* **6**, 034005 (2016).
- [80] F. T. Tabesh, Q. Hassanzada, M. Hadian, A. Hashemi, I. A. Sarsari, and M. Abdi, Strain induced coupling and quantum information processing with hexagonal boron nitride quantum emitters, *Quantum Science and Technology* **7**, 015002 (2022).
- [81] G. Grosso, H. Moon, B. Lienhard, S. Ali, D. K. Efetov, M. M. Furchi, P. Jarillo-Herrero, M. J. Ford, I. Aharonovich, and D. Englund, Tunable and high-purity room temperature single-photon emission from atomic defects in hexagonal boron nitride, *Nature Communications* **8**, 705 (2017).
- [82] T. Wah, Vibration of circular plates, *J. Acoust. Soc. Am.* **34**, 275 (1962).
- [83] A. M. Van Der Zande, R. A. Barton, J. S. Alden, C. S. Ruiz-Vargas, W. S. Whitney, P. H. Pham, J. Park, J. M. Parpia, H. G. Craighead, and P. L. McEuen, Large-scale arrays of single-layer graphene resonators, *Nano Letters* **10**, 4869 (2010).
- [84] C. Di Giorgio, E. Blundo, G. Pettinari, M. Felici, F. Bobba, and A. Polimeni, Mechanical, Elastic, and Adhesive Properties of Two-Dimensional Materials: From Straining Techniques to State-of-the-Art Local Probe Measurements, *Advanced Materials Interfaces* **9**, 2102220 (2022).
- [85] X. Zhang, K. Makles, L. Colombier, D. Metten, H. Majjad, P. Verlot, and S. Berciaud, Dynamically-enhanced strain in atomically thin resonators, *Nature Communications* **11**, 5526 (2020).
- [86] I. Wilson-Rae, P. Zoller, and A. Imamoglu, Laser Cooling of a Nanomechanical Resonator Mode to its Quantum Ground State, *Physical Review Letters* **92**, 075507 (2004).
- [87] C. Freysoldt, B. Grabowski, T. Hickel, J. Neugebauer, G. Kresse, A. Janotti, and C. G. Van De Walle, First-principles calculations for point defects in solids, *Reviews of Modern Physics* **86**, 253 (2014).
- [88] Á. Gali, Recent advances in the ab initio theory of solid-state defect qubits, *Nanophotonics* **12**, 359 (2023).
- [89] C. Freysoldt, J. Neugebauer, and C. G. Van De Walle, Fully Ab initio finite-size corrections for charged-defect supercell calculations, *Physical Review Letters* **102**, 016402 (2009).
- [90] M. H. Naik and M. Jain, Coffee: Corrections for formation energy and eigenvalues for charged defect simulations, *Computer Physics Communications* **226**, 114 (2018).